Oriented Growth of Gold Nanowires on MoS_2

*Daisuke Kiriya, Yuzhi Zhou, Christopher Nelson, Mark Hettick, Surabhi Rao Madhvapathy, Kevin Chen, Peida Zhao, Mahmut Tosun, Andrew M. Minor, Daryl C. Chrzan, and Ali Javey**

Layered 2D materials serve as a new class of substrates for templated synthesis of various nanomaterials even with highly dissimilar crystal structures; thus overcoming the lattice constraints of conventional epitaxial processes. Here, molybdenum disulfide (MoS_2) is used as a prototypical model substrate for oriented growth of in-plane Au nanowires (NWs) despite the nearly 8% lattice mismatch between MoS_2 and Au. Au NWs on the MoS_2 surface are oriented along three symmetrically equivalent directions within the substrate arising from the strong Au–S binding that templates the oriented growth. The kinetics of the growth process are explored through experiments and modeling. Strong charge transfer is observed between Au NWs and MoS_2, resulting in degenerate p-doping of MoS_2.

1. Introduction

The ability of one material to influence the crystallography of another at an interface is the foundation for constructing functional heterojunctions for a myriad of electronic, energy, and photonic applications. The ultimate limit of this process is epitaxy, whereby the second material, usually a thin layer, fully adopts the planar interface symmetry of the host substrate. Metal nanostructures with an epitaxial growth mode on semiconducting compounds[1] and metal oxides[2] have been widely studied for use in catalytic,[2a,b] plasmonic,[1a,2d] and nanoelectronic[1d,3] devices. Morphologies of the metal nanostructures should be taken into consideration to maximize the properties of the metal surface. In general, morphologies such as spheres (particles),[1d,4] platelets (squares, triangles etc),[1c,e] and vertically aligned pillars[5] have been systematically generated. Since the interface of the junction is often a 2D crystalline plane with high symmetry, growth of anisotropic shapes, such as horizontal nanowires (NWs), on the plane can be difficult. Previously, in-plane oriented epitaxial growth of Si,[6] metal oxide,[7] and III–V NWs[8] have been demonstrated via the vapor–liquid–solid (VLS) process with metal nanoparticles as catalysts. In the conventional epitaxial growth process, the crystal structure and lattice constants of the substrates and grown material need to be closely matched. Here, we explore the use of layered materials as template substrates for oriented growth of in-plane metal NWs. As a proof of concept, we demonstrate growth of in-plane oriented Au NWs with *C*3 symmetry on molybdenum disulfide (MoS_2) surfaces. The rich surface chemistry of MoS_2 with weakly bonded layered structure facilitates the oriented growth of Au NWs despite the highly mismatched crystal structures of Au and MoS_2 with a large lattice mismatch of 8%. This work presents a unique platform for growth of highly dissimilar heterostructures using layered substrates; overcoming the lattice constraints of conventional epitaxial processes. Furthermore, we demonstrate degenerate p-doping of MoS_2 as a result of charge transfer with the Au NWs.

Transition metal dichalcogenides (TMDCs) are promising materials for the next generation electro-optical devices due to their atomically thin layered nature,[9] variety of band gaps ranging from metallic to insulating depending on the combination of metals and chalcogenide atoms,[10] relatively high carrier mobilities (≈200 $cm^2\ V^{-1}\ s^{-1}$ for WSe_2)[11] and in some cases, high thermal and chemical stabilities[10,12] for device fabrication processing. The bonding within each layer of TMDCs is ionic/covalent while the adjacent layers are coupled via van der Waals (vdW) interactions. Due to this weak interlayer binding and very smooth surface, vdW epitaxy has been proposed to form functional crystals on the surface of layered materials.[13] Previously, vdW epitaxy of various 2D layered materials based on a combination of TMDCs, h-BN, and graphene has been reported.[13a,14,15] Since the interaction with the substrate is not strong, the vdW epitaxy has mainly generated 2D symmetric crystals due to the laterally highly-symmetrical plane at the

Dr. D. Kiriya, M. Hettick, S. R. Madhvapathy, K. Chen, P. Zhao, M. Tosun, Prof. A. Javey
Electrical Engineering and Computer Sciences
University of California
Berkeley, CA 94720, USA
E-mail: ajavey@berkeley.edu

Dr. D. Kiriya, Y. Zhou, M. Hettick, S. R. Madhvapathy, K. Chen, P. Zhao, M. Tosun, Prof. D. C. Chrzan, Prof. A. Javey
Materials Sciences Division
Lawrence Berkeley National Laboratory
Berkeley, CA 94720, USA

Dr. D. Kiriya, M. Hettick, K. Chen, P. Zhao, M. Tosun, Prof. A. Javey
Berkeley Sensor and Actuator Center
University of California
Berkeley, CA 94720, USA

Y. Zhou, Prof. A. M. Minor, Prof. D. C. Chrzan
Materials Science and Engineering
University of California
Berkeley, CA 94720, USA

Dr. C. Nelson, Prof. A. M. Minor
National Center for Electron Microscopy
Molecular Foundry
Lawrence Berkeley National Laboratory
Berkeley, CA 94720, USA

DOI: 10.1002/adfm.201502582

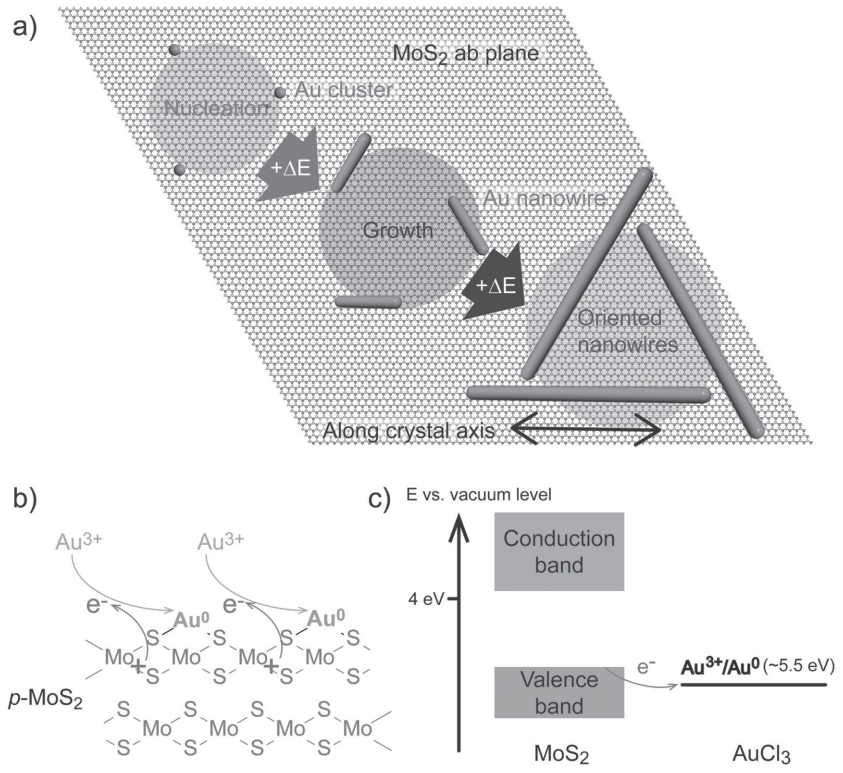

Figure 1. a) Schematic illustration of the growth of the in-plane oriented Au NWs on the MoS_2 surface. By casting $AuCl_3$ solution, Au atoms are supplied on the surface of MoS_2 (*ab* plane). Au atoms diffuse to form nuclei on the surface and eventually generate NWs by application of thermal energy. The NWs are in-plane oriented, reflecting the hexagonal lattice of the *ab* plane MoS_2. b) Schematic illustration of the redox reaction between Au^{3+} and MoS_2 to form an Au^0–MoS_2 complex. c) Qualitative energy diagram between MoS_2 and $AuCl_3$. The reduction potential of Au^{3+}/Au^0 is ≈5.5 eV (vs vacuum level). Since the valence band edge of MoS_2 is less than ≈5.5 eV, electron transfer from MoS_2 to Au^{3+} occurs.

junction of the inorganic crystals.[13,14] Here, we use MoS_2 as a model TMDC substrate to grow in-plane Au NWs despite the nearly 8% lattice mismatch between MoS_2 and Au. Au NWs on the MoS_2 surface are oriented along three symmetrically equivalent directions within the substrate arising from the strong Au–S binding that templates the oriented growth. A strong charge transfer reaction with MoS_2 is observed through electrical measurements, resulting in degenerate p-doping of MoS_2.

2. Results and Discussion

Figure 1a shows an illustrative image of the growth of Au NWs from nucleation to growth on the surface of MoS_2. Casting $AuCl_3$ solution onto MoS_2 supplies Au atoms on the surface. To form Au NWs on MoS_2, we cast a 30 wt% $AuCl_3$ solution in diluted HCl (Sigma-Aldrich) onto a mechanically exfoliated MoS_2 flake for 1 min and then blow off the extra solution with N_2 gas followed by annealing at 150 °C for 2 min on a hot plate in an ambient environment. During the thermal annealing process, Au atoms on the surface aggregate to form nuclei and further assemble to form NWs. Uniquely, the NWs are oriented with *C3* symmetry, suggesting coherence with the threefold symmetry[10] of the surface of MoS_2. Previous works have demonstrated self-assembled monolayers (SAM) of alkyl thiol molecules (R-SH) on Au surfaces.[16] In the SAM case, a strong interaction between S and Au facilitates the formation of the monolayer of thiolate molecules on top of Au.[16] The structure shown in Figure 1a is similar but opposite from the usual SAMs; Au atoms are instead assembled onto the S lattice of MoS_2. $AuCl_3$ was chosen as an Au source because it has a high reduction potential (≈5.5 eV vs vacuum level).[17] With the valence band edge of MoS_2 less than ≈5.5 eV, a redox reaction between $AuCl_3$ and MoS_2 would occur spontaneously on the surface (Figure 1b,c) to supply Au atoms effectively.[10b,17a] Previously, formation of Au nanoparticles on MoS_2 has been reported using a similar $AuCl_3$ treatment.[1c,d,4,17a,18] Stimulated from the research, in-plane oriented Au NW formation was targeted in this research.

Figure 2a,b shows atomic force microscopy (AFM) images of a 6.4 nm thick MoS_2 flake before and after the $AuCl_3$ treatment, respectively. NWs are clearly observed on the surface after $AuCl_3$ treatment and thermal annealing. The length of the NWs is ≈500 nm with a diameter of ≈10 nm from the AFM observations. Since no NWs were observed on the surface of SiO_2 (Figure 2b), the growth of the NWs is expected to be controlled by the interaction between Au^{3+} and MoS_2. The NW formation is independent of MoS_2 flake thickness: NWs can also be formed on bilayers (1.5 nm thick, Figure 2c) and monolayers (0.7 nm thick, Figure 2d) of MoS_2. We analyzed the statistical distribution of the angles of the NWs shown in a 2.5 μm × 2.5 μm area (Figure 2d). We found that NWs were well oriented with peak distributions at approximately every 60°, along the ≈40°, 95°, and 154° directions, indicating the *C3* symmetry orientation (Figure 2e). Given the consideration of the *C3* symmetry of the *ab* plane of MoS_2 (Figure 1a) and no NW formation on the SiO_2 surface, the NW growth is strongly influenced from the MoS_2 substrate which is also suggested from the nuclei preferentially oriented along a lattice of MoS_2 (vide infra).

We further analyzed the effect of the $AuCl_3$ concentration and deposition time on NW morphology. Decreasing the concentration of $AuCl_3$ from 30 to 1 wt% by dilution with Milli-Q water decreases the diameter of NWs (d) from d = 17.5 nm (30 wt%) to d = 6.5 nm (1 wt%) (**Figure 3**a–d and Figure S1, Supporting Information) using the same deposition procedures as previously described (1 min deposition followed by 150 °C annealing for 2 min). Higher concentrations facilitate more Au deposition on the surface, leading to the generation of thicker Au NWs. We also found that there is a critical concentration for the generation of NWs based on the 1 min deposition procedure. Below 0.5 wt%, nanoparticles are formed instead (Figure 3e). However, by using a longer deposition time, even the 0.5 wt% $AuCl_3$ can be used to generate NWs (Figure 3f).

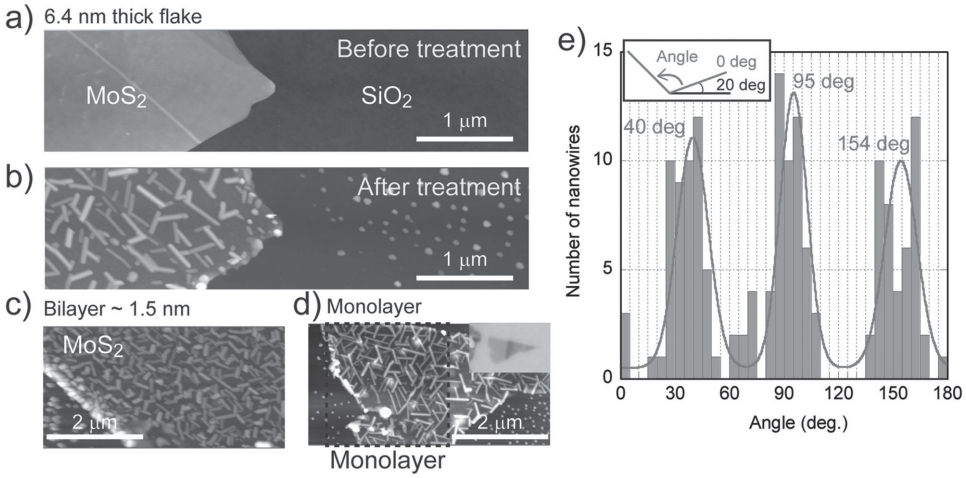

Figure 2. Demonstration of the oriented growth of Au NWs on MoS_2 surface. AFM images of an exfoliated MoS_2 flake (6.8 nm thickness) a) before and b) after Au NW growth on the surface. AFM images of Au NWs on c) bilayer and d) monolayer MoS_2. All samples were treated with a 30 wt% $AuCl_3$ solution followed by thermal annealing at 150 °C. e) Statistical distribution of the orientation angle of Au NWs on monolayer MoS_2 in (d). NWs are oriented at approximately every 60°. This orientation trend reflects the hexagonal symmetry of the MoS_2 *ab* surface. The histogram is fitted with three Gaussian distributions (red solid line).

This result also follows from the above discussion, indicating a critical amount of Au on MoS_2 needed to generate NWs. A longer deposition time of 60 min shows a similar distribution of Au NWs (≈10 nm thickness) as in the 10 min case (Figure 3g), indicating saturation of Au coverage on the MoS_2 surface by $AuCl_3$ treatment. Upon heating, these Au atoms diffuse and nucleate clusters. Higher concentrations lead to a higher nucleation rate for Au clusters. Faster growth rates are also expected for high concentration solutions.

Assembly of Au atoms on MoS_2 is found to show various morphologies from nanoparticles to NWs depending on the annealing conditions. Importantly, the NWs can be formed only in a limited annealing temperature condition. This is also observed under AFM before/after annealing of a MoS_2 flake treated with $AuCl_3$. Features were not observed before thermal annealing while on the other hand, NWs were clearly generated after annealing at 150 °C for 5 min (Figure S2, Supporting Information). **Figure 4**a shows a growth morphology diagram of Au on MoS_2 with various annealing times/temperatures. At the lower temperature region (below 100 °C), Au shows up only as small nanoparticles on MoS_2 (≈4 nm, Figure S3, Supporting Information). Increasing the temperature above 130 °C results in NW formation, suggesting that surface diffusion of Au is important to generate NWs (Figures S4 and S5, Supporting Information). With further annealing (either higher temperature or longer annealing time) the NWs display a pearling instability, and decompose into lines of Au nanoparticles (Figures S4–S6, Supporting Information). The above phase transformations are illustrated in Figure 4b. We speculate that after the deposition of $AuCl_3$ on MoS_2, both atomic Au and unreacted $AuCl_3$ molecules (vide infra) are present on the surface (Figure 4bi). Applying thermal energy ($\Delta E1$) to the complex induces diffusion of these species to form nuclei (nucleation, Figure 4bii). With increased annealing time/temperature and correspondingly, more thermal energy ($\Delta E2$), nucleation is completed and NWs are grown (Figure 4biii). More energy ($\Delta E3$) induces transformation of NWs into a sequence of nanoparticles and eventually coagulation of each nanoparticle to form a large particle by additional energy ($\Delta E4$). The observation of NW growth suggests an anisotropic growth rate along different Au crystalline facets. While the exact mechanism is intriguing and not well established, the presence of ions would play a critical role in the NW growth, similar to previously reported solution phase synthesis of NW growth.[19] The importance of $AuCl_3$ existence on the MoS_2 surface is confirmed from a control experiment with evaporated Au (0 valence gold) that resulted in platelet structures instead of NWs after thermal annealing (Figure S7, Supporting Information). The *C*3 symmetry of the NW growth orientation suggests strong binding interaction between Au and S atoms on the surface of MoS_2. Thus, despite the different crystal structure and large lattice mismatch (≈8%) of the two materials, the MoS_2 substrate acts as an effective template in guiding the orientation of the grown NWs on the surface.

The mechanism by which the MoS_2 substrate templates the growth process is not fully understood. Efforts to observe directly the relevant interface have been thwarted by the instability of the wires in the presence of an electron beam and/or light. When exposed to these forms of radiation, the NWs display a pearling instability and form Au clusters (as noted in Figure 4). One possible origin of the templating is that the wires are growing via vdW epitaxy.[20] In this case, the growing wires would continue to feel the atomic scale corrugation of the substrate through the weak vdW bonding between the substrate and the wires, yielding a preferred orientation. Alternatively, more traditional epitaxy is also a possibility. As mentioned above, the lattice mismatch for {111} oriented growth is approximately 8% biaxially. (The lattice mismatch for {001} oriented growth would introduce lower, but still significant strain in the growing film.) Nevertheless, transmission electron microscopy (TEM) studies of the growth of Au on MoS_2, performed in situ, resulted in Au platelets that grew epitaxially on the substrate

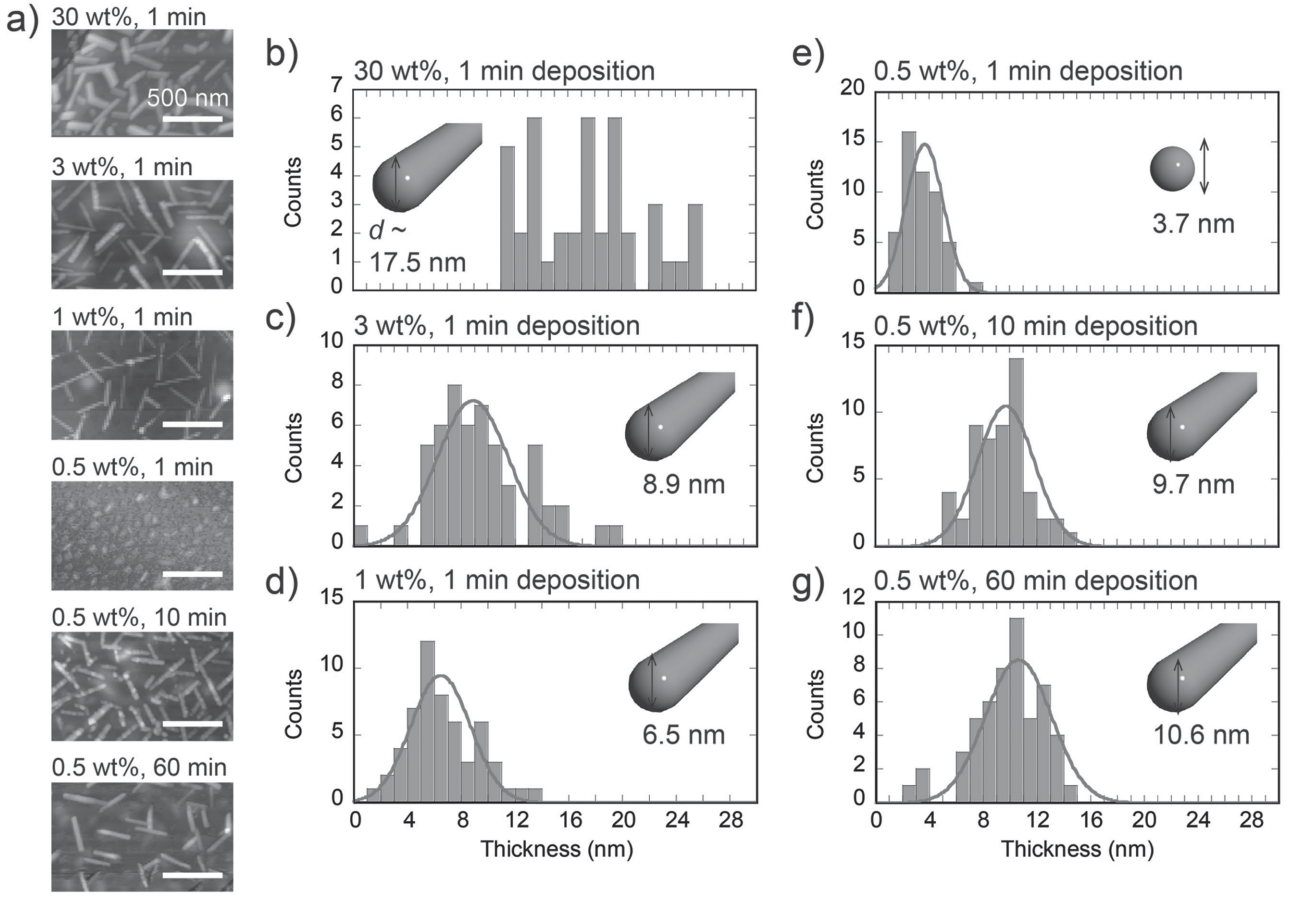

Figure 3. Concentration dependency of $AuCl_3$ on NW formation. a) AFM images of Au NWs/nanoparticles on MoS_2 obtained from treatment with various $AuCl_3$ concentrations followed by thermal annealing at 150 °C for 2 min. Concentrations and deposition times are labeled above each image. b–g) Histograms of the diameter of Au nanostructures obtained from $AuCl_3$ depositions with b) 30 wt% for 1 min, c) 3 wt% for 1 min, d) 1 wt% for 1 min, e) 0.5 wt% for 1 min, f) 0.5 wt% for 10 min, and g) 0.5 wt% for 60 min. Except for the case of 0.5 wt% for 1 min, all other conditions result in the formation of NWs. Red solid lines in the histograms are Gaussian fitting lines. In the case of the 30 wt% for 1 min case, the fitting failed due to the high dispersity.

(most likely with the introduction of misfit dislocations).[21] A recent theoretical analysis suggests that {111} oriented epitaxy is favored by the strength of the Au–S bond at the interface, and the elastic compliance of the MoS_2 substrate.[22] Similar factors could be influencing the growth of the NWs, and an epitaxial relationship would help to explain the preferred growth direction.

To characterize the state of the Au clusters on MoS_2, we carried out X-ray photoelectron spectroscopy (XPS) analysis (**Figure 5**a,b). Figure 5a presents Au core levels (4f) from the treatment with 30 wt% $AuCl_3$ solution followed by thermal annealing as shown in Figure 2. The four peaks observed correspond to Au^{3+} and Au^0 doublets, with both $4f_{7/2}$ and the indicated $4f_{5/2}$ components fit as Voight lineshapes.[23] The peak area ratio corresponding to $4f_{5/2}$ of Au^{3+} to Au^0 is ≈23%. This suggests that close to 80% of the Au^{3+} is converted into Au^0 on the MoS_2 surface, indicating strong electron transfer between MoS_2 and Au^{3+}. Figure 5b indicates the core levels of Cl (2p) on the same sample. Two types of Cl species are observed, corresponding to Cl–Au species originating in $[AuCl_4]^-$ and Cl atoms on MoS_2 which would be in the form of Cl^- ions[23,24] From the relative area of each Cl core level peak, we estimate ≈30% of the total Cl atoms are Cl^- ions on MoS_2. According to these results, the surface is mostly coated with elemental Au clusters with measurable $[AuCl_4]^-$ content. The X-ray diffraction (XRD) analysis in Figure S8 (Supporting Information) further identifies the assembly of crystalline Au on MoS_2 after $AuCl_3$ treatment and annealing.

The preferential crystallographic alignment of some of the Au nanoparticle nuclei prior to Au NW growth was observed by selected area electron diffraction (SAED) using TEM (Figure S9, Supporting Information). SAED diffraction patterns were taken from multiple Au nanoparticles on a free-standing MoS_2 flake and exhibited diffraction peaks consistent with *d*-spacings of the bulk Au fcc phase. A consistent preferred orientation was not apparent for this sample size (≈20 particles), but aligned diffraction peaks were observed for $Au\{220\}\|MoS_2(\bar{1}\bar{1}0)$, $Au\{311\}\|MoS_2(\bar{2}10)$, $Au\{111\}\|MoS_2(100)$, and $Au\{200\}\|MoS_2(310)$. Given the variety of observed orientations and noting that not all particles in the set had visible diffraction peaks nor did any appear to share a principle zone axis with MoS_2, the MoS_2 surface in the TEM study did not

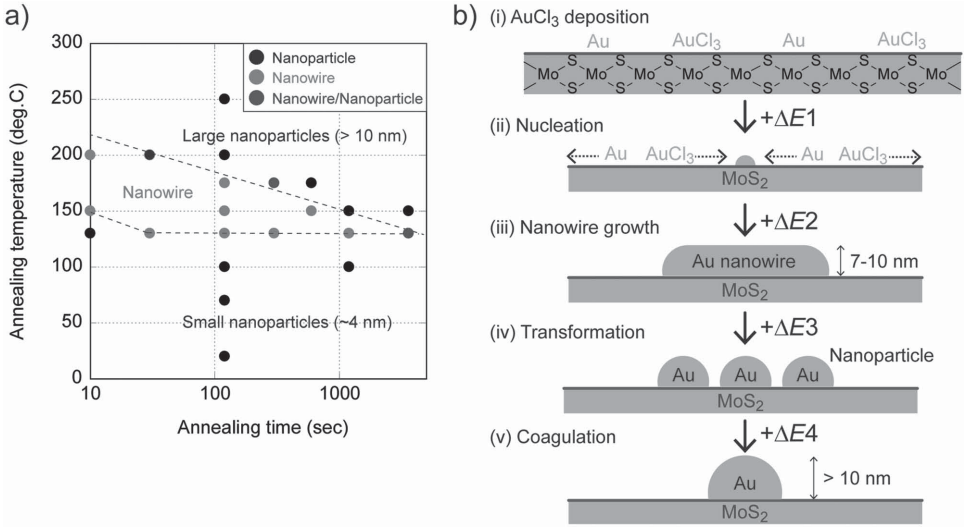

Figure 4. a) Growth morphology diagram of Au nanostructures on MoS_2 as a function of annealing time and temperature (with a 3 wt% $AuCl_3$ solution casted for 1 min). NWs are generated in a limited range (temperatures between 130 to 200 °C and annealing time below 1 h). b) Plausible transformation of Au nanostructures on MoS_2 as a function of thermal energy. i) Casting of $AuCl_3$ solution on MoS_2 supplies Au on MoS_2. Applying additional energy ($\Delta E1$ to $\Delta E4$) induces ii) nucleation from Au atoms by $\Delta E1$, iii) nanowire generation by $\Delta E2$, iv) a transformation of NWs into a set of nanoparticles by $\Delta E3$, and v) coagulation of nanoparticles into large particles by $\Delta E4$.

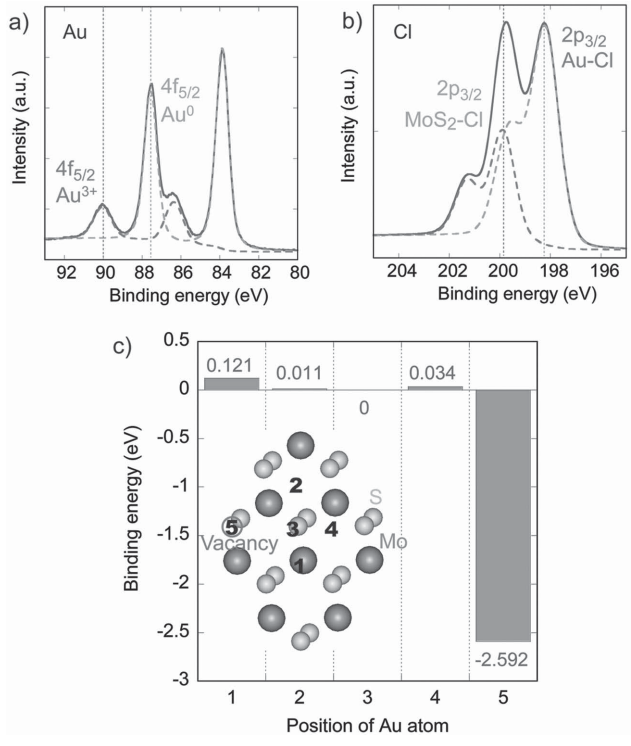

Figure 5. Characterization of Au on MoS_2. XPS spectra for a) Au core levels ($4f_{7/2}$ and $4f_{5/2}$) and b) Cl core levels ($2p_{3/2}$ and $2p_{1/2}$) for an MoS_2 sample after treatment with a 30 wt% $AuCl_3$ for 1 min followed by annealing at 150 °C for 2 min. c) Relative binding energy obtained from DFT simulations for an Au atom on various MoS_2 positions. The energy for the Au on S atom of MoS_2 is set as 0 eV. Each position is defined as follows. 1: Au on top of Mo; 2: Au on an interstitial site of the hexagonal lattice; 3: Au on S; 4: Au on an interstitial site between two S atoms; and 5: Au on S vacancy.

appear to strongly enforce a crystallographic orientation of the Au nuclei. However, wherever the gold planes were visible by SAED they exhibited preferential orientation to a nearby MoS_2 plane. Unfortunately, a similar TEM study of NWs could not be performed due to pearling instability of the wires under the electron beam converting the NWs into nanoparticles.

Theoretical simulation using density functional theory (DFT) was also applied to better understand the nucleation from the interaction between Au atom and MoS_2 on the surface (Figure 5c and Supporting information). Compared to Au atom on the S atom of MoS_2, Au atom on the Mo atom of MoS_2 shows a higher energy (0.12 eV). The result is as expected; Au and S atoms have higher affinity. Another important point is that the binding energy of Au atom on S vacancies was found to be −2.6 eV. This interaction is found to be thermodynamically very strong, which would be the main nucleation site for Au clusters.

To analyze the electrical properties of MoS_2 after the generation of Au NWs, we examined the transfer characteristics of back gated MoS_2 field-effect transistors (FETs). FETs were fabricated by mechanically exfoliating ≈100 nm thick MoS_2 flakes on 260 nm SiO_2 on a heavily doped p^+-Si wafer as a universal back gate (**Figure 6**a,b). Photolithography is used to define source and drain electrodes followed by evaporation of Au/Cr (40/0.5 nm). The channel length of the devices is 10 µm. Figure 6a and Figure S10 (Supporting Information) show transfer characteristic curves (drain voltage (V_{DS}) = +1 or −1 V for n and p type characteristics, respectively) before/after treatment of 1 wt% $AuCl_3$ on the device. The pristine device shows n-type behavior as similar to previous reports. After the treatment of the $AuCl_3$, the polarity of the device changes from n-type to p-type and the ON current level monotonically increases several orders of magnitude (≈10^3) with increasing deposition time of the $AuCl_3$. Previously, a report demonstrated

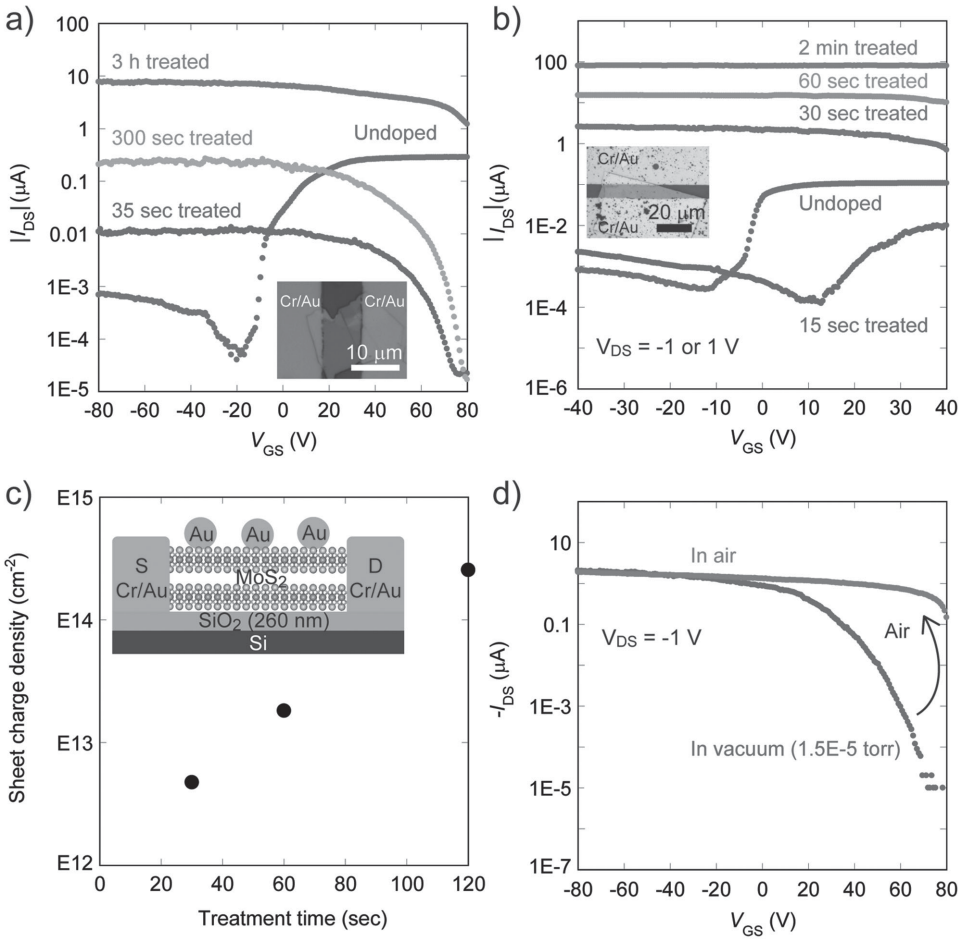

Figure 6. Electrical characterization of MoS_2 after Au NW growth. a) Characteristic transfer curves after each sequential treatment (1 wt% $AuCl_3$ solution followed by annealing at 150 °C for 2 min each) for a device with 95 nm thick MoS_2. The pristine MoS_2 shows n-type behavior and adding the treatment (from 35 s to 3 h) switches the polarity and increases the ON current level. Inset shows an optical microscope image of the device used for this experiment. V_{DS} = +1 or −1 V for before and after $AuCl_3$ treatment, respectively. b) A similar treatment study as shown in Figure 6a using a 30 wt% $AuCl_3$ solution and an MoS_2 flake with 114 nm thickness. c) Sheet hole density in the Au decorated MoS_2 devices as a function of $AuCl_3$ deposition time. The charge density monotonically increases with the $AuCl_3$ deposition time to 2.5×10^{14} cm^{-2} after 2 min. d) Environmental effect on the doping of MoS_2 by Au NWs. The thickness of the flake is 29 nm. When placed in ≈10^{-5} Torr vacuum, the transfer characteristic curve shows strong gate dependency with ON/OFF ≈10^5 (blue curve) arising from reduced doping. After reexposure to air, the curve goes back to the degenerately doped state with no gate dependence (red curve). The ambient effect arises from the known sensitivity of the Au work function to H_2O and O_2.

$AuCl_3$ can act as an acceptor; the polarity transformation in our case is comparable.[25] As discussed in Figure 3e,f, since a longer deposition time increases the surface coverage of Au on MoS_2, the hole concentration of MoS_2 is also increased as the deposition time increases. Interestingly, in the case of using 30 wt% $AuCl_3$ solution (Figure 6b), just a 30 s treatment shows a drastic change in the electrical properties, resulting in small V_{GS} dependency, corresponding to a degenerately doped p^+ situation. Treatments longer than 30 s increase I_{DS} monotonically. From these characteristic curves, we extracted the sheet charge density (n_{2D}) using the Equation (1).[26]

$$n_{2D} = (I_{DS}L) / (qWV_{DS}\mu) \quad (1)$$

where q is the electron charge, W and L represent width and length of the channel, respectively, I_{DS} is the drain current at V_{GS} = 0 V, V_{DS} is the source to drain bias, and μ is the field-effect hole mobility. We used W = 45 μm by averaging the width of the two source and drain metal contacts. As shown in Figure 6c, the carrier density increases with increasing doping time to 2.5×10^{14} cm^{-2} at 120 s. Previously, NO_2 was used as a p-type degenerate dopant for WSe_2, with a doping concentration ceiling of ≈ 10^{13} cm^{-2}.[11] The growth of Au on the surface of MoS_2 also induces the high carrier concentration due to its effective surface charge transfer interaction.

When measured under vacuum (≈10^{-5} Torr), the degenerate p-doped state of Au doped MoS_2 converts into a nondegenerate state with an ON/OFF ratio over 10^5 (Figure 6d). A reexposure of the device back to ambient environment immediately reverses the transfer characteristic back to a representative p^+-type degenerate state without gate dependency. From these results, we attribute work function modulation of the Au due to air adsorbates as responsible for the demonstrated reversible transfer characteristic between the degenerate state and

nondegenerate states. Previously, devices with carbon nanotubes (CNTs) as a channel material showed similar reversible transfer characteristics.[27] The work function of Au is easily affected by adsorbates such as water and oxygen, and in our case, these adsorbates would change the work function of the Au NWs (and nanoparticles) on MoS_2.[28] As a control experiment, since the solution of $AuCl_3$ is HCl-based, we examined a similar back gated MoS_2 device treated with HCl only (Figure S11, Supporting Information). Although the ON current level was increased by annealing due to changes in the metal contact, the polarity of MoS_2 was maintained to be *n*-type, signaling the doping is due to the $AuCl_3$ and not the HCl.

3. Conclusions

In summary, we demonstrate in-plane oriented growth of Au NWs with *C*3 symmetry on layered MoS_2 substrates by deposition of $AuCl_3$ solutions and thermal annealing. Despite the large difference in the crystal structure of the two materials, MoS_2 surface serves as an effective template substrate in guiding the oriented growth of Au NWs. Preliminary theoretical studies suggest the process is facilitated by the layered structure of MoS_2 which allows for mechanical compliance of its top surface layer, and the strong S–Au binding. The work suggests a new crystal growth platform by using layered substrates to overcome the crystal lattice constraints of conventional epitaxial processes.

4. Experimental Section

Fabrication of the Devices: The devices shown in Figure 6 were fabricated via standard photolithographic techniques. Source and drain metal pads (Cr/Au = 0.5/40 nm) were made via electron beam evaporation followed by lift-off.

Treatment of $AuCl_3$ onto MoS_2: The preparation of Au NWs was done with the following procedures. First, MoS_2 flakes were exfoliated via mechanical exfoliation onto an Si wafer with 260 nm of thermal oxide. $AuCl_3$ solution ($AuCl_3$ in HCl, Sigma Aldrich) was then dropcast onto the MoS_2 flake and subsequently blown off with dry N_2 gas. Finally, the sample was annealed at 150 °C for several minutes (usually 2 min). The test of $AuCl_3$ concentrations ranged from 0.5 to 30 wt%, diluted with Milli-Q water from an original concentration of 30 wt%. For electrical measurements (Figure 6), the $AuCl_3$ treatment was done after fabrication of the back gated devices.

Supporting Information

Supporting Information is available from the Wiley Online Library or from the author.

Acknowledgements

This work was supported by the Director, Office of Science, Office of Basic Energy Sciences, Material Sciences and Engineering Division of the US Department of Energy under Contract No. DE-AC02-05CH11231. The device fabrication and characterization was funded by the Center for Low Energy Systems Technology (LEAST), one of six centers supported by the STARnet phase of the Focus Center Research Program (FCRP), a Semiconductor Research Corporation program sponsored by MARCO and DARPA. The transmission electron microscopy and XRD were performed at the Molecular Foundry, supported by the Office of Science, Office of Basic Energy Sciences, of the U.S. Department of Energy under Contract No. DE-AC02-05CH11231. XPS characterization was performed at the Joint Center for Artificial Photosynthesis, supported through the Office of Science of the US Department of Energy under Award Number DE-SC0004993.

Received: June 23, 2015
Revised: August 13, 2015
Published online: September 16, 2015

[1] a) Y. J. Lu, J. Kim, H. Y. Chen, C. H. Wu, N. Dabidian, C. E. Sanders, C. Y. Wang, M. Y. Lu, B. H. Li, X. G. Qiu, W. H. Chang, L. J. Chen, G. Shvets, C. K. Shih, S. Gwo, *Science* **2012**, *337*, 450; b) W. L. Shi, H. Zeng, Y. Sahoo, T. Y. Ohulchanskyy, Y. Ding, Z. L. Wang, M. Swihart, P. N. Prasad, *Nano Lett.* **2006**, *6*, 875; c) X. Huang, Z. Y. Zeng, S. Y. Bao, M. F. Wang, X. Y. Qi, Z. X. Fan, H. Zhang, *Nat. Commun.* **2013**, 4; d) Y. M. Shi, J. K. Huang, L. M. Jin, Y. T. Hsu, S. F. Yu, L. J. Li, H. Y. Yang, *Sci. Rep.* **2013**, 3; e) G. Honjo, K. Yagi, J. Vac. *Sci. Technol.* **1969**, *6*, 576.

[2] a) V. Komanicky, H. Iddir, K. C. Chang, A. Menzel, G. Karapetrov, D. Hennessy, P. Zapol, H. You, *J. Am. Chem. Soc.* **2009**, *131*, 5732; b) C. Wang, H. Daimon, S. H. Sun, *Nano Lett.* **2009**, *9*, 1493; c) F. R. Fan, Y. Ding, D. Y. Liu, Z. Q. Tian, Z. L. Wang, *J. Am. Chem. Soc.* **2009**, *131*, 12036; d) Z. X. Chen, B. Y. Lai, J. M. Zhang, G. P. Wang, S. Chu, *Nanotechnology*, **2014**, *25*.

[3] a) J. Schornbaum, B. Winter, S. P. Schiessl, F. Gannott, G. Katsukis, D. M. Guldi, E. Spiecker, J. Zaumseil, *Adv. Funct. Mater.* **2014**, *24*, 5798; b) C. H. Lee, T. Schiros, E. J. G. Santos, B. Kim, K. G. Yager, S. J. Kang, S. Lee, J. Yu, K. Watanabe, T. Taniguchi, J. Hone, E. Kaxiras, C. Nuckolls, P. Kim, *Adv. Mater.* **2014**, *26*, 2812.

[4] L. H. Yuwen, F. Xu, B. Xue, Z. M. Luo, Q. Zhang, B. Q. Bao, S. Su, L. X. Weng, W. Huang, L. H. Wang, *Nanoscale* **2014**, *6*, 5762.

[5] a) R. S. Wagner, W. C. Ellis, *Appl. Phys. Lett.* **1964**, *4*, 89; b) P. D. Yang, H. Q. Yan, S. Mao, R. Russo, J. Johnson, R. Saykally, N. Morris, J. Pham, R. R. He, H. J. Choi, *Adv. Funct. Mater.* **2002**, *12*, 323.

[6] L. W. Yu, M. K. Xu, J. Xu, Z. G. Xue, Z. Fan, G. Picardi, F. Fortuna, J. Z. Wang, J. Xu, Y. Shi, K. J. Chen, P. R. I. Cabarrocas, *Nano Lett.* **2014**, *14*, 6469.

[7] D. Tsivion, M. Schvartzman, R. Popovitz-Biro, E. Joselevich, *ACS Nano* **2012**, *6*, 6433.

[8] a) D. Tsivion, M. Schvartzman, R. Popovitz-Biro, P. von Huth, E. Joselevich, *Science* **2011**, *333*, 1003; b) S. A. Fortuna, J. G. Wen, I. S. Chun, X. L. Li, *Nano Lett.* **2008**, *8*, 4421.

[9] Y. Yoon, K. Ganapathi, S. Salahuddin, *Nano Lett.* **2011**, *11*, 3768.

[10] a) M. Chhowalla, H. S. Shin, G. Eda, L. J. Li, K. P. Loh, H. Zhang, *Nat. Chem.* **2013**, *5*, 263; b) M. Tosun, D. Fu, S. B. Desai, C. Ko, J. S. Kang, D.-H. Lien, M. Najmzadeh, S. Tongay, J. Wu, A. Javey, *Sci. Rep.* **2015**, *5*, 10990.

[11] H. Fang, S. Chuang, T. C. Chang, K. Takei, T. Takahashi, A. Javey, *Nano Lett.* **2012**, *12*, 3788.

[12] B. Radisavljevic, A. Radenovic, J. Brivio, V. Giacometti, A. Kis, *Nat. Nanotechnol.* **2011**, *6*, 147.

[13] a) Y. J. Hong, W. H. Lee, Y. P. Wu, R. S. Ruoff, T. Fukui, *Nano Lett.* **2012**, *12*, 1431; b) H. Oh, Y. J. Hong, K. S. Kim, S. Yoon, H. Baek, S. H. Kang, Y. K. Kwon, M. Kim, G. C. Yi, *NPG Asia Mater.* **2014**, *6*, e145.

[14] a) H. Ago, H. Endo, P. Solís-Fernández, R. Takizawa, Y. Ohta, Y. Fujita, K. Yamamoto, M. Tsuji, *ACS Appl. Mater. Int.* **2015**, *7*, 5265; b) Y. M. Shi, W. Zhou, A. Y. Lu, W. J. Fang, Y. H. Lee, A. L. Hsu, S. M. Kim, K. K. Kim, H. Y. Yang, L. J. Li, J. C. Idrobo,

J. Kong, *Nano Lett.* **2012**, *12*, 2784; c) P. K. Mohseni, A. Behnam, J. D. Wood, C. D. English, J. W. Lyding, E. Pop, X. L. Li, *Nano Lett.* **2013**, *13*, 1153.
[15] W. C. Lee, K. Kim, J. Park, J. Koo, H. Y. Jeong, H. Lee, D. A. Weitz, A. Zettl, S. Takeuchi, *Nat. Nanotechnol.* **2015**, *10*, 423.
[16] a) H. Häkkinen, *Nat. Chem.* **2012**, *4*, 443; b) W. S. Liao, S. Cheunkar, H. H. Cao, H. R. Bednar, P. S. Weiss, A. M. Andrews, *Science*, **2012**, *337*, 1517.
[17] a) J. Kim, S. Byun, A. J. Smith, J. Yu, J. X. Huang, *J. Phys. Chem. Lett.* **2013**, *4*, 1227; b) K. K. Kim, J. J. Bae, H. K. Park, S. M. Kim, H. Z. Geng, K. A. Park, H. J. Shin, S. M. Yoon, A. Benayad, J. Y. Choi, Y. H. Lee, *J. Am. Chem. Soc.* **2008**, *130*, 12757.
[18] a) T. S. Sreeprasad, P. Nguyen, N. Kim, V. Berry, *Nano Lett.* **2013**, *13*, 4434; b) S. Su, H. F. Sun, F. Xu, L. H. Yuwen, L. H. Wang, *Electroanal.* **2013**, *25*, 2523.
[19] Y. N. Xia, Y. J. Xiong, B. Lim, S. E. Skrabalak, *Angew. Chem. Int. Ed.* **2009**, *48*, 60.
[20] A. Koma, *Thin Solid Films* **1992**, *216*, 72.
[21] D. W. Pashley, M. J. Stowell, M. H. Jacobs, T. J. Law, *Philos. Mag.* **1964**, *10*, 127.
[22] Y. Zhou, D. Kiriya, E. E. Haller, J. W. Ager, A. Javey, D. C. Chrzan, arXiv:1505.07505, **2015**.
[23] S. M. Kim, K. K. Kim, Y. W. Jo, M. H. Park, S. J. Chae, D. L. Duong, C. W. Yang, J. Kong, Y. H. Lee, *ACS Nano* **2011**, *5*, 1236.
[24] S. Jung, J. T. Han, J. S. Woo, J. H. Kim, H. J. Jeong, G. W. Lee, *Nanoscale* **2014**, *6*, 2971.
[25] M. S. Choi, D. Qu, D. Lee, X. Liu, K. Watanabe, T. Taniguchi, W. J. Yoo, *ACS Nano*, **2014**, *8*, 9332.
[26] H. Fang, M. Tosun, G. Seol, T. C. Chang, K. Takei, J. Guo, A. Javey, *Nano Lett.* **2013**, *13*, 1991.
[27] I. Lee, U. J. Kim, H. Bin Son, S. M. Yoon, F. Yao, W. J. Yu, D. L. Duong, J. Y. Choi, J. M. Kim, E. H. Lee, Y. H. Lee, *J. Phys. Chem. C* **2010**, *114*, 11618.
[28] R. L. Wells, T. Fort, *Surf. Sci.* **1972**, *32*, 554.

ADVANCED FUNCTIONAL MATERIALS

Supporting Information

for *Adv. Funct. Mater.*, DOI: 10.1002/adfm.201502582

Oriented Growth of Gold Nanowires on MoS_2

*Daisuke Kiriya, Yuzhi Zhou, Christopher Nelson, Mark Hettick, Surabhi Rao Madhvapathy, Kevin Chen, Peida Zhao, Mahmut Tosun, Andrew M. Minor, Daryl C. Chrzan, and Ali Javey**

Supporting Information

Oriented Growth of Gold Nanowires on MoS_2

Daisuke Kiriya, Yuzhi Zhou, Christopher Nelson, Mark Hettick, Surabhi Rao Madhvapathy, Kevin Chen, Peida Zhao, Mahmut Tosun, Andrew M. Minor, Daryl C. Chrzan and Ali Javey[*]

Sample preparation for TEM observation

A MoS_2 flake was transferred onto a Si plate (a thin Si plate (~5 μm thickness) with 2 μm diameter holes) by a dry transfer technique (Ref. S1). The transferred flake was suspended on the hole in the plate. The flake was treated with a diluted $AuCl_3$ solution (0.5 wt%) for just several seconds (ca. 2 sec) and the extra liquid was sucked away with a paper cloth. Since the flake was in a suspended situation, dry N_2 gas blow was not used to remove the extra liquid to avoid any mechanical stresses that might damage the flake. The short treatment time was applied to reduce the probability of forming too many or stacked nuclei on the MoS_2. To form the nucleus, the treated sample was kept in a dry N_2 environment at r.t. for 1 month to grow it gradually in order to avoid annealing at a high temperature which may induce mechanical stress to the MoS_2 flake which can dissociate the flake on the Si plate.

Characterization

Optical microscope images are taken using an Olympus BX51 equipped with a digital camera (Olympus, QCOLOR3). Electrical measurements are done with an HP 4155C analyzer. Electrical measurements in vacuum (Figure 6d) are done with a vacuum probe station (Lake Shore Cryotronics Inc.). AFM observations are done with a Nanoscope Dimension 3100 atomic force microscope (Digital Instruments Inc.). XPS measurements are performed with a Kratos AXIS Ultra DLD system with a hemispherical analyzer and monochromatic Al Kα source, and fits were performed using typical Voigt lineshapes, a Shirley background, and

spin-orbit splitting values and ratios typical of the respective 4f and 2p orbitals. XRD patterns were taken on a Bruker AXS D8 Discover GADDS XRD Diffractometer system.

Transmission electron microscopy in Figure S9 was obtained by an FEI Titan microscope operating at 80 kV. The nanoparticles were confirmed to be chemically Au using energy dispersive x-ray spectroscopy. Selected Area Electron Diffraction (SAED) patterns were captured for regions with Au nanoparticles, and a reference MoS_2 SAED pattern was captured from an immediately adjacent region. Difference images were created by subtraction of raw SAED patterns taken with identical exposures and the result was normalized symmetrically about zero to a range of -1 to 1 using identical scaling parameters for all images so they remain directly comparable. Au and MoS_2 peak d-spacings were measured by Gaussian fit and d-spacings where by calibrated to the MoS_2 peaks using a value of d = 2.73 Å for (100) peaks. The Au peaks in Figure S9 had measured d-spacings of 2.36 Å , 1.98 Å, 1.40 Å, and 1.30 Å, which are close fits to nominal Au d-spacings for {111} (d = 2.35 Å), {200} (d = 2.03 Å), {220} (d = 1.44 Å), and {311} (d = 1.23 Å) planes.

DFT simulations

The DFT calculations are performed using the plane-wave code VASP [Ref.S2]. The exchange and correlation energy is described by the generalized gradient approximation (GGA) proposed by Perdew, Burke, and Ernzerhof (PBE) [Ref.S3]. Electron-ion interactions are treated with projector augmented wave (PAW) potentials [Ref.S4]. All calculations are performed using a plane-wave basis with a 280 eV energy cutoff. The van der Waals (vdW) interaction is also included following Grimme's D2 method [Ref.S5]. The convergence criterion for self-consistent field (SCF) loop is 1×10^{-6} eV. The building block to construct the supercell is the rectangular unit cell of MoS_2 which contains two primitive unit cells. The monolayer supercell contains 72 unit cells with a total of 216 atoms. The Au adatom (or molecule) is then placed onto different positions of the monolayer. A 50 Å vacuum slab is

added along the direction normal to the monolayer to ensure the separation of the system with its periodic boundary image and also the accuracy of vdW corrections. The Brillioun zone is sampled at the Γ point. Atomic positions are relaxed until the maximum Hellmann-Feynman force on any atom was below 0.01 eV/Å.

After relaxation, the Au adatoms in different positions stay close to the MoS_2 monolayer (all about 2 Å away from the monolayer). Their relative stability is further summarized in Figure 5c. For Au adatoms on perfect monolayer MoS_2, their stability can be directly compared from their total energies. The S top position (indicated by "3" in Figure 5c) is the most energetically favorable site of perfect monolayer MoS_2. For Au adatom in S vacancy, we further calculate the total energy of the system where the Au atom is displaced 20 Å away from the monolayer (still with a S vacancy). The energy difference between that of the original system (Au in S vacancy) quantitatively reflects the stability of Au in S vacancy. Similar calculations are done for Au on a perfect MoS_2 monolayer. In this way, we can compare Au on perfect MoS_2 and Au in S vacancy even though the numbers of S atoms are different.

References

[Ref.S1] H. Fang *et al. Proc. Natl. Acad. Sci.* **2014**, *111*, 6198.

[Ref.S2] G. Kresse and J. Hafner, *Phys. Rev. B*, **1993**, *47*, 558.

[Ref.S3] J. P. Perdew, K. Burke, and M. Ernzerhof, *Phys. Rev. Lett*. **1996**, *77*, 3865.

[Ref.S4] G. Kresse and D. Joubert, *Phys. Rev. B*, **1999**, *59*, 1758.

[Ref.S5] S. Grimme, Journal of Computational Chemistry, **2006**, 27, 1787.

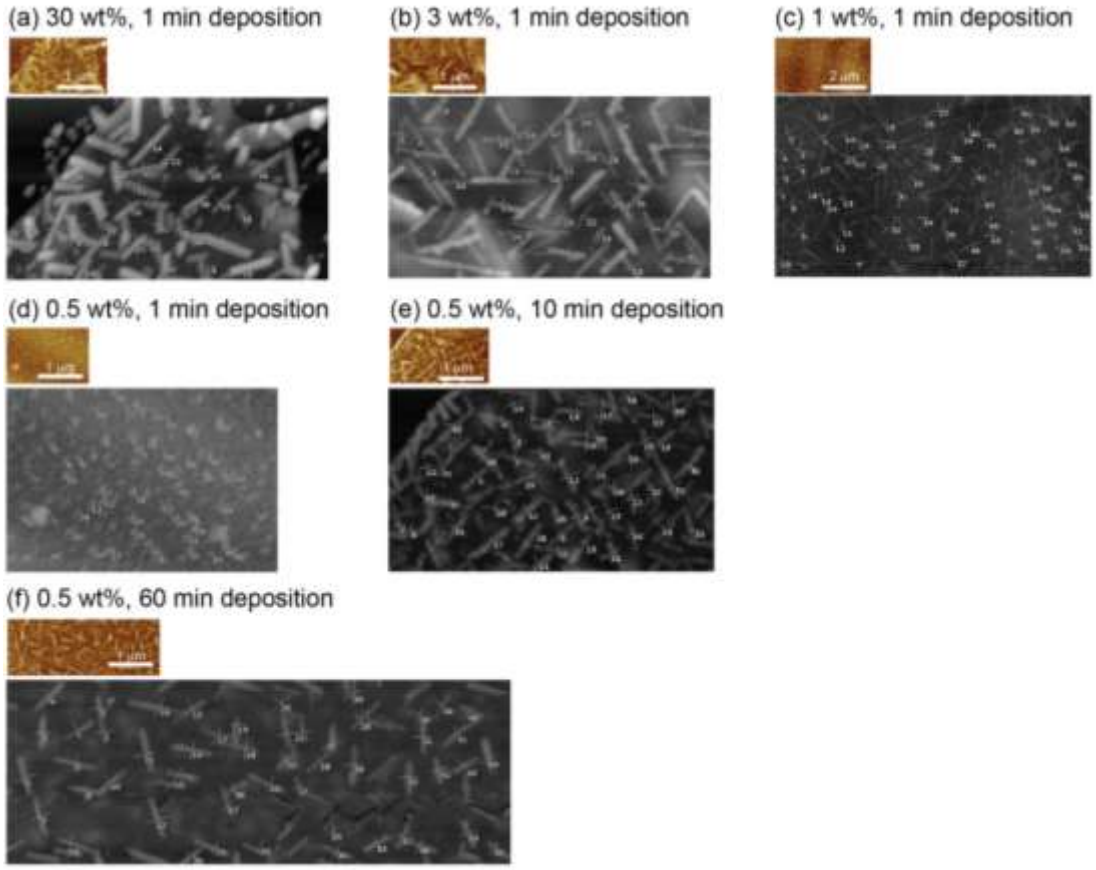

Figure S1. AFM images (top) with corresponding reference images indicating the positions at which line scans were taken to determine NW diameters for the histograms shown in Figure 3. The samples are treated with (a) 1 min deposition of 30 wt% $AuCl_3$ solution, (b) 1 min deposition of 3 wt% $AuCl_3$ solution, (c) 1 min deposition of 1 wt% $AuCl_3$ solution, (d) 1 min deposition of 0.5 wt% $AuCl_3$ solution, (e) 10 min deposition of 0.5 wt% $AuCl_3$ solution, and (f) 60 min deposition of 0.5 wt% $AuCl_3$ solution. After the deposition of $AuCl_3$ solution, all samples are blown with dry N_2 gas to remove extra solution followed by annealing at 150 °C for 2 min.

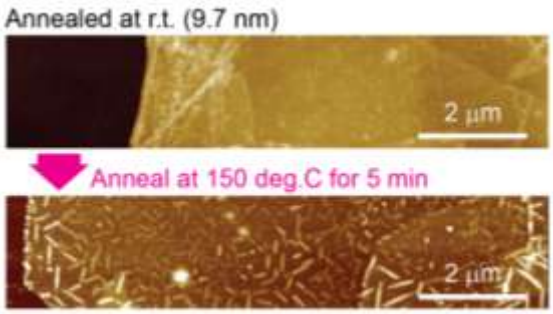

Figure S2. AFM images before/after annealing the $AuCl_3$ treated MoS_2. In the top image no texture was observed on the MoS_2 flake (9.7 nm thickness) after 3 wt% $AuCl_3$ deposition for 1 min followed by N_2 blow dry of the solution. As shown in the bottom image however, after annealing the sample at 150 °C for 5 min, Au nanowires formed on the surface.

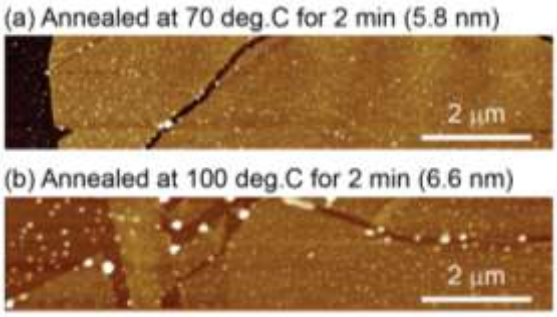

Figure S3. AFM images for MoS_2 flakes after treatments of 3 wt% $AuCl_3$ for 1 min followed by N_2 blow dry and annealing at (a) 70 °C for 2 min and (b) 100 °C for 2 min. No nanowires were generated and tiny Au dots are observed on the MoS_2 in both cases. The flake thicknesses are shown in parentheses above each image.

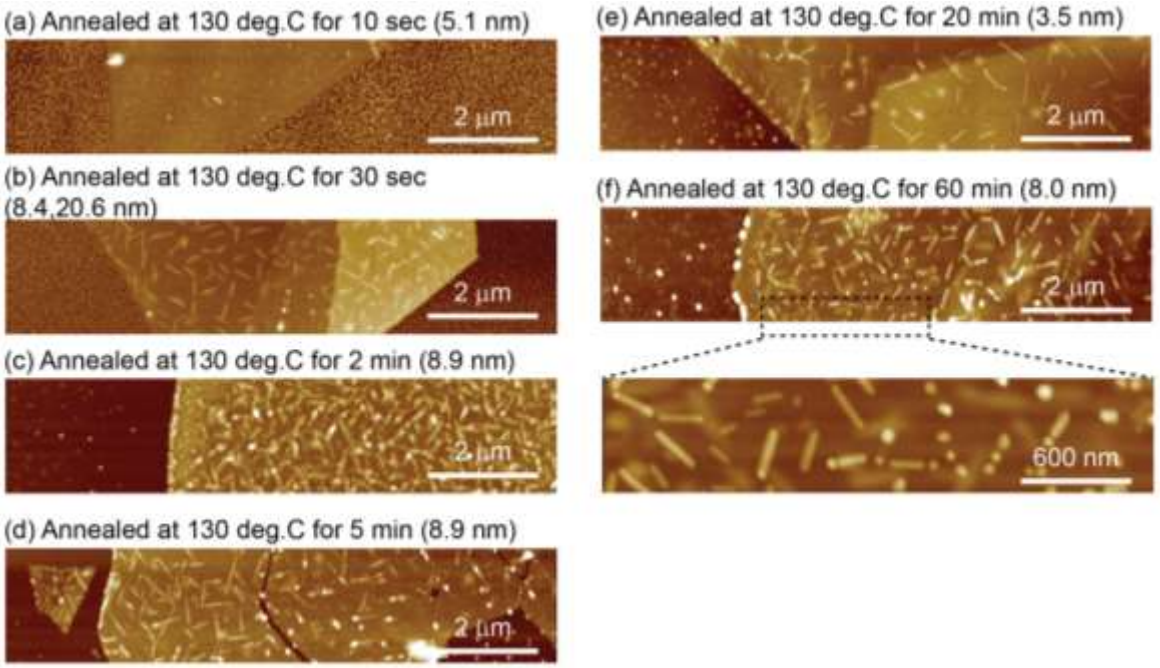

Figure S4. AFM images for MoS_2 flakes after treatments of 3 wt% $AuCl_3$ for 1 min followed by N_2 blow dry and annealing at (a) 130 °C for 10 sec, (b) 130 °C for 30 sec, (c) 130 °C for 2 min, (d) 130 °C for 5 min, (e) 130 °C for 20 min, and (f) 130 °C for 60 min. The flake thicknesses are shown in parentheses above each image. Transformation of nanowires into nanoparticles is observed in Figure S4f.

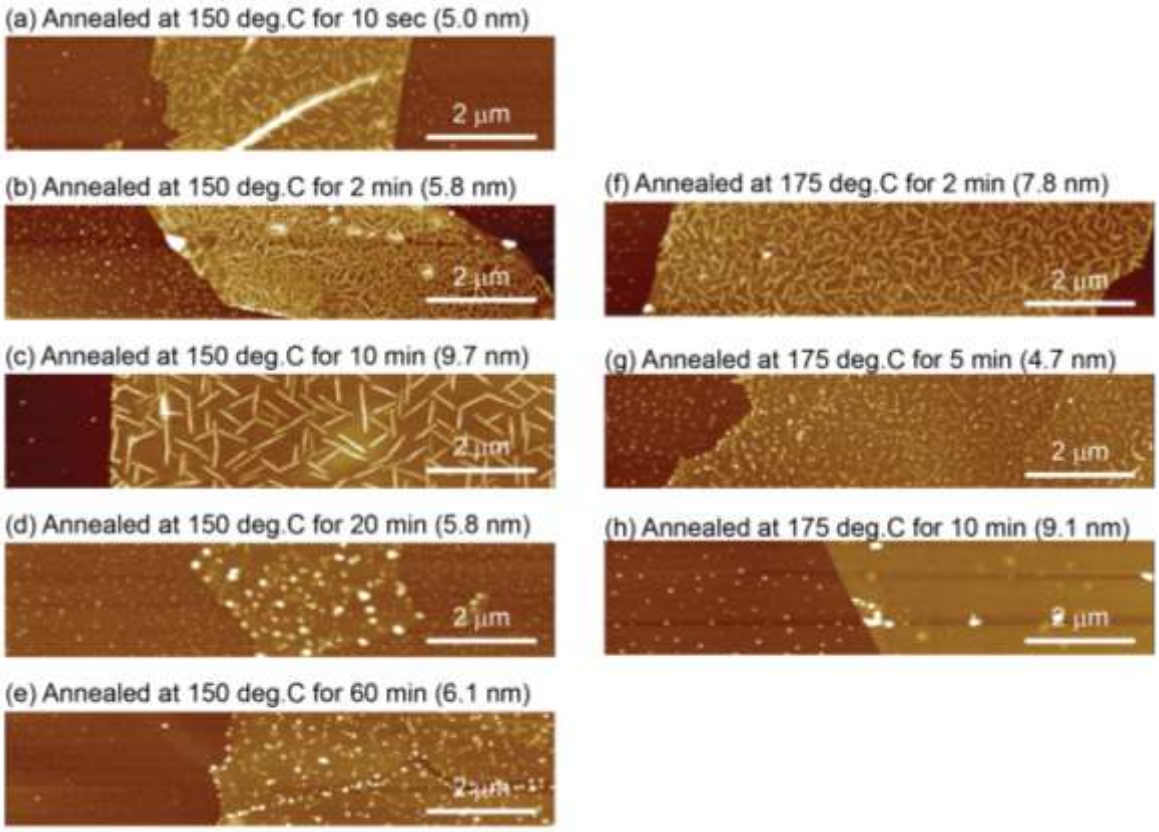

Figure S5. AFM images for MoS_2 flakes after treatments of 3 wt% $AuCl_3$ for 1 min followed by N_2 blow dry and annealing at (a) 150 °C for 10 sec, (b) 150 °C for 2 min, (c) 150 °C for 10 min, (d) 150 °C for 20 min, (e) 150 °C for 60 min, (f) 175 °C for 2 min, (g) 175 °C for 5 min, and (h) 175 °C for 10 min. The flake thicknesses are shown in parentheses above each image. Transformation of nanowires into nanoparticles starts after 5 min annealing at 175 °C as shown in Figure S5g and completely changes after 10 min as shown in Figure S5h.

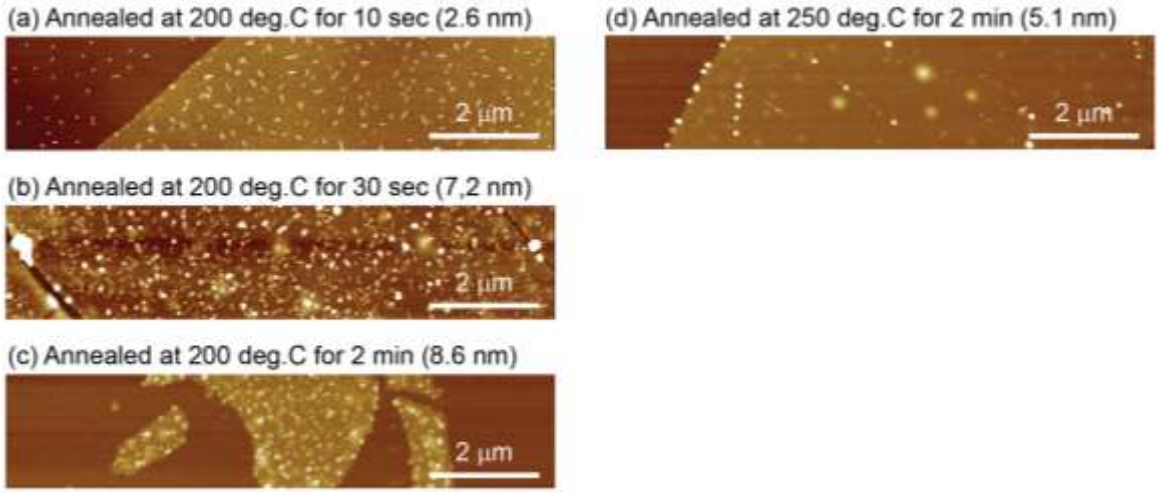

Figure S6. AFM images for MoS_2 flakes after treatments of 3 wt% $AuCl_3$ for 1 min followed by N_2 blow dry and annealing at (a) 200 °C for 10 sec, (b) 200 °C for 30 sec, (c) 200 °C for 2 min, and (d) 250 °C for 2 min. The flake thicknesses are shown in parentheses above each image. Transformation of nanowires into nanoparticles starts after 30 sec annealing at 200 °C as shown in Figure S6b.

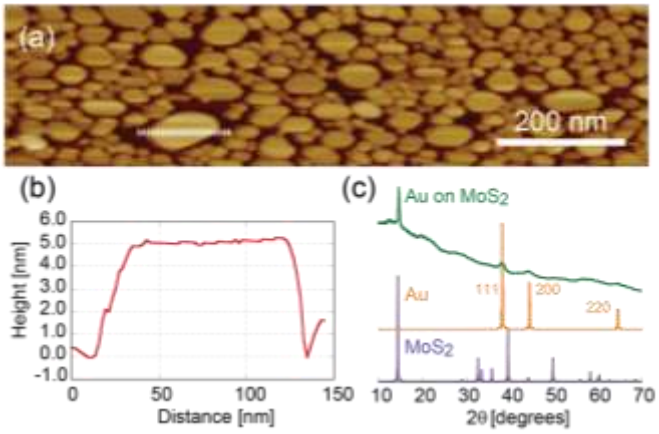

Figure S7. Au structure from e-beam evaporation of Au (2 nm) on MoS_2. The structure was obtained after annealing in forming gas (5% H_2/95% N_2) at 400°C for 2 min. (a) The AFM image of the evaporated Au on MoS_2 flakes after the annealing. Hexagonal platelet structures were observed. (b) A line profile on the dotted line in Figure S7a. A flat surface was confirmed. (c) XRD pattern of the evaporated Au structure on the MoS_2.

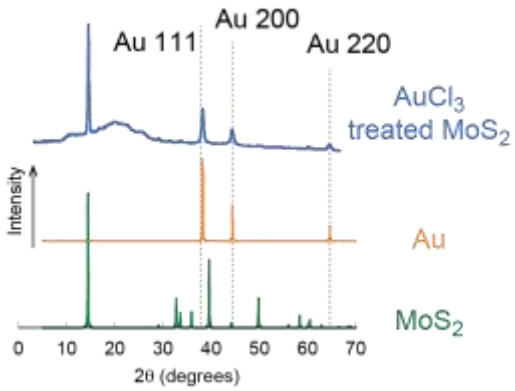

Figure S8. XRD pattern for a $AuCl_3$ treated MoS_2 sample (blue curve). Simulated patterns for MoS_2 (green curve) and Au (orange) are also shown. A broad peak around 20 degrees shown in the treated MoS_2 is from carbon tape underneath. Diffraction patterns are from Cif file of MoS_2 (9007660) is from Crystallography Open Database and Au (9008463) is from Crystallography Open Database.

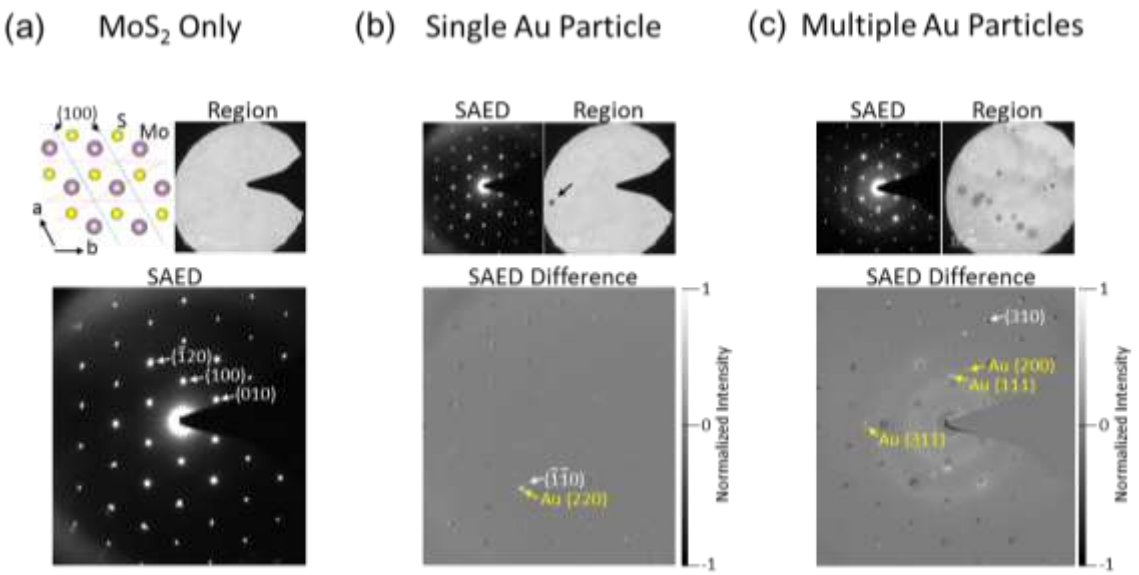

Figure S9. Preferential alignments of Au nanoparticles on a MoS_2 surface is shown by TEM selected area electron diffraction (SAED) patterns. TEM images and diffraction patterns are taken from a free-standing MoS_2 flake after treatment with 0.5 wt% $AuCl_3$ solution. (a) The SAED pattern from a reference region of bare MoS_2 is shown with several of the principle planes labeled, taken from the circular region shown in the TEM image at the top right. The corresponding MoS_2 crystal structure for a single layer of the hexagonal P 63/mmc 2H polytype is depicted top left with the same three planes highlighted. (b) The SAED pattern for a region containing a single Au nanoparticle and the corresponding TEM image of this region are shown at top left and right respectively. The Au diffraction peaks are highlighted by subtracting the SAED pattern of bare MoS_2. In this case an Au peak with a d-spacing of 1.4 Å consistent with Au{220} planes (d = 1.44 Å) is shown aligned to the MoS_2 $(\bar{1}\bar{1}0)$ peak. These two distinct peaks appearing in-line indicates that they are coplanar but with separate d-spacings consistent with a preferential alignment between these planes. (c) An SAED pattern (top left) taken from a region with multiple Au particles (top right) is shown with the Au peaks highlighted by again subtracting the SAED pattern from bare MoS_2. Multiple aligned Au and MoS_2 planes are present and labeled: Au{311}||$MoS_2(\bar{2}10)$, Au{111}||$MoS_2(100)$, and Au{200}||$MoS_2(310)$.

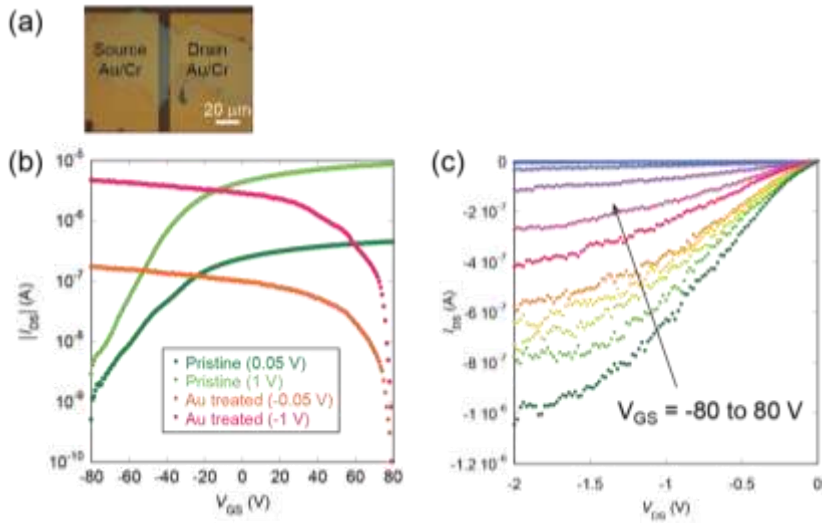

Figure S10. Electronic property of the MoS_2 flake after 1 wt% $AuCl_3$ deposition for 5 min followed by N_2 blowdry and 150 °C annealing for 2 min. (a) An optical microscope image of the device. The thickness of the flake is 90 nm. (b) Transfer characteristics of the pristine device (before treatment) and after treatment of the $AuCl_3$ solution at drain voltages of 0.05 V (dark green) and 1 V (light green) for the pristine and -0.05 V (orange) and -1 V (red) for the $AuCl_3$ treated. (c) Output characteristics for the $AuCl_3$ treated sample. The gate voltage (V_{GS}) is varied from -80 V to 80 V with 10 V increments.

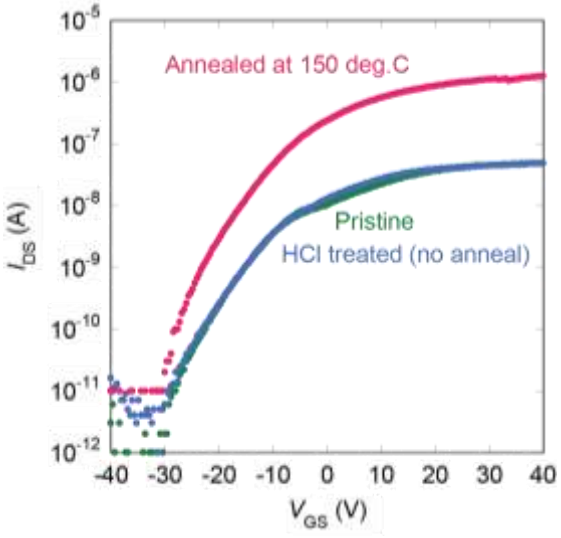

Figure S11. Control experiment to confirm HCl effect for transfer characteristics of MoS_2. The device is similar to the one shown in Figure S10. Transfer characteristics of the pristine MoS_2 device (green), after deposition of 1.2 M HCl for 1 min (blue), and after annealing the HCl treated device at 150 °C for 2 min (red). Drain voltages are 1 V in all cases. The current level is increased after annealing at 150 °C due to improvements in the metal contacts. All of them show *n*-type behavior.